Supporting information

Potential-Dependent Active Moiety of Fe-N-C Catalysts for the Oxygen Reduction Reaction

Kang Liu,[†,‡] Junwei Fu,[‡] Tao Luo,[‡] Ganghai Ni,[‡] Hongmei Li,[‡,§] Li Zhu,[∥] Ye Wang,[⊥] Zhang Lin,[†,*] Yifei Sun,[⊥,#,*] Emiliano Cortés,[∥,*] and Min Liu[‡,*]

[†]School of Metallurgy and Environment, Central South University, Changsha 410083, Hunan, P. R. China

[‡]Hunan Joint International Research Center for Carbon Dioxide Resource Utilization, School of Physics and Electronics, Central South University, Changsha 410083, Hunan, P. R. China

[§]School of Materials Science and Engineering, Zhengzhou University, Zhengzhou 450001, Henan, P. R. China

[∥]Nanoinstitute Munich, Faculty of Physics, Ludwig Maximilians Universität München, 80539 München, Germany

[⊥]School of Energy and Power Engineering, Beihang University, Beijing 100191, China

[#]Research Center for Advanced Energy and Carbon Neutrality, Beihang University, Beijing 100191, China

Corresponding Authors: Z.L.: zhang_lin@csu.edu.cn, Y.S.: sunif@buaa.edu.cn, E.C.: Emiliano.Cortes@lmu.de, and M.L.: minliu@csu.edu.cn

1. Computational method

Our spin-polarized density functional theory (DFT) calculations were performed by using the Vienna ab initio simulation package (VASP).[1-2] The projector augmented wave (PAW) method was employed to describe the interaction of electron-ion.[3] The generalized gradient approximation (GGA) of Perdew–Burke–Ernzerhof (PBE) was used to treat the electron-electron exchange and correlation functional.[4-5] We used the effective Hubbard-U parameter of 3 eV for Fe 3d orbitals.[6-8] The cutoff energy was set to 400 eV. A 2 × 2 × 1 Monkhorst–Pack k-point mesh was used for the k-space integration. van der Waals (VDW) forces were corrected with the D2 method of Grimme.[9] The convergence thresholds for force and energy were 0.02 eV $Å^{-1}$ and 1 × 10^{-5} eV/atom respectively. We built a super-cell (7 × 8) carbon substrate as a model, which includes 106 C atoms, 4 N atoms, and 1 Fe atom. The lattice parameters of this slab are a = 17.31 Å and b = 16.98 Å after optimization. The vacuum layer was set at 15 Å. We used the implicit solvent model of VASPsol to deal with solvent effects in our calculations.[10-11] The Debye length was set to 3Å to simulate the experimental acid conditions (1M). The dielectric constant for water was set to a relative permittivity value of 80. The structures of different spin states were obtained at zero charges by the occupation matrix control plugin for VASP.[12] In constant potential calculations, the wave function of the spin state at zero charges is read as the initial wave function for optimization.

Constant-potential calculations were applied using the code freely available from Duan and Xiao.[13] At the applied potential (U) on the standard hydrogen electrode (SHE)

scale, the number of electrons and the atomic coordinates of the system are optimized simultaneously. The chemical potential of the electron ($\bar{\mu_e}$) is calculated as

$$\bar{\mu_e} = \mu_{e,\mathrm{SHE}} + U \qquad (1)$$

where $\mu_{e,\mathrm{SHE}}$ is the electronic chemical potential of the system relative to the SHE.

$$\mu_{e,\mathrm{SHE}} = E_f/\mathrm{e} - V_{sol} + \varphi_0/\mathrm{e} \qquad (2)$$

where E_f is the Fermi level, V_{sol} is the potential deep in the solution, and $\varphi_0 = -4.6$ eV for the SHE. The grand canonical energy of the system is defined as

$$\Omega = E_{\mathrm{DFT}} + \Delta n \bullet (U - V_{sol} + \varphi_0/\mathrm{e}) \qquad (3)$$

where E_{DFT} is the energy calculated from the DFT and Δn is the number of electrons added or removed from the system.

The chemical potential of the electron ($\bar{\mu_e}$) is derived as

$$\mu_e = \partial\Omega/\partial n = E_f/\mathrm{e} - V_{sol} + \varphi_0/\mathrm{e} + U \qquad (4)$$

The Gibbs free energy can be expressed as

$$\mathrm{G} = \Omega + \mathrm{ZPE} - \mathrm{T} \bullet \mathrm{S} \qquad (5)$$

where Ω, ZPE, and S are the grand canonical energy, the zero-point energies, and the entropy of the system, respectively.[14-16] T is the temperature (298.15 K, in our work).

The limiting potential is defined as

$$\mathrm{U_L} = -\Delta \mathrm{G_{max}}/\mathrm{e} \qquad (6)$$

where $\Delta \mathrm{G_{max}}$ is the free energy change of the potential-determining step in the ORR process.

The free energy of OH^- is deduced from the following half-reaction potentials

$$\mathrm{O_2} + 4\mathrm{H^+} + 4\mathrm{e} = 2\mathrm{H_2O} \qquad (\mathrm{E^0} = 1.229\ \mathrm{V}) \qquad (7)$$

$$\mathrm{O_2} + 2\mathrm{H^+} + 4\mathrm{e} = \mathrm{H_2O_2} \qquad (\mathrm{E^0} = 0.682\ \mathrm{V}) \qquad (8)$$

$$H_2O_2 + 4e = 2OH^- \qquad (E^0 = 0.880\ V) \qquad (9)$$

where E^0 (*vs.* SHE) is the formal redox potential for various reactions.

The adsorption energy (E_{ads}) of the adsorbate on the substrate is calculated as:

$$E_{ads} = E_{total} - E_{adsorbate} - E_{substrate} \qquad (10)$$

where E_{total} is the total energy of the adsorbed system, $E_{adsorbate}$ is the energy of the free adsorbate, and $E_{substrate}$ is the pure substrate energy.

The electron occupancy of the Fe 3d projection orbital (*n*) is expressed as:

$$n = \int_{-\infty}^{0} n(\varepsilon)d\varepsilon \qquad (11)$$

where $n(\varepsilon)$ is the Fe 3d projected density of states. *n* also represents the number of electrons in the occupied state.

2. Results and discussion

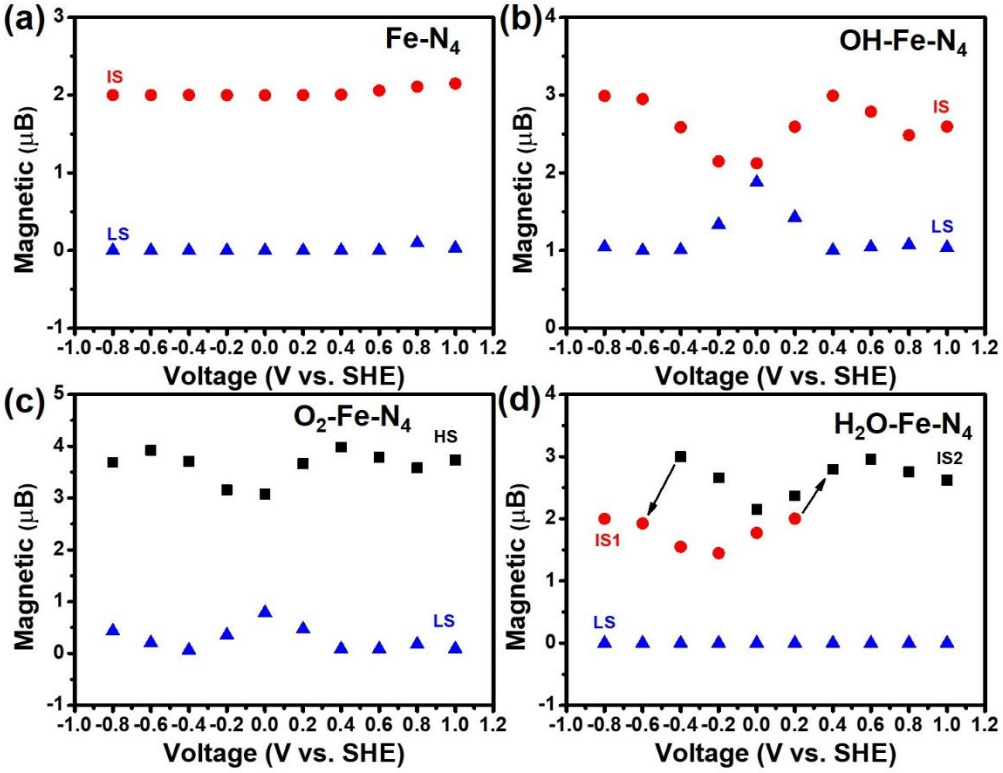

Figure S1. The spin moment for various spin states of Fe-N_4 (a), OH-Fe-N_4 (b), O_2-Fe-N_4 (c), and H_2O-Fe-N_4 (d) systems at different potentials.

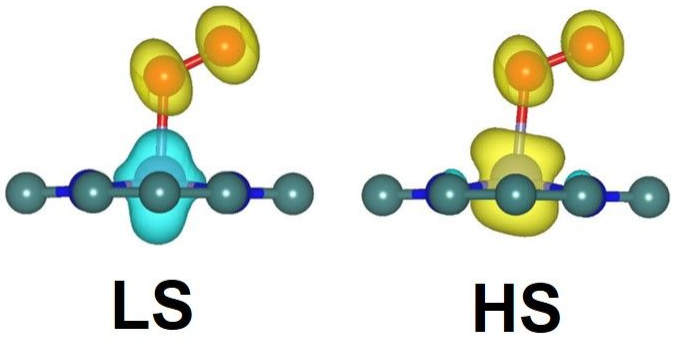

Figure S2. The spin density of the O_2-Fe-N_4 system at the LS and HS states.

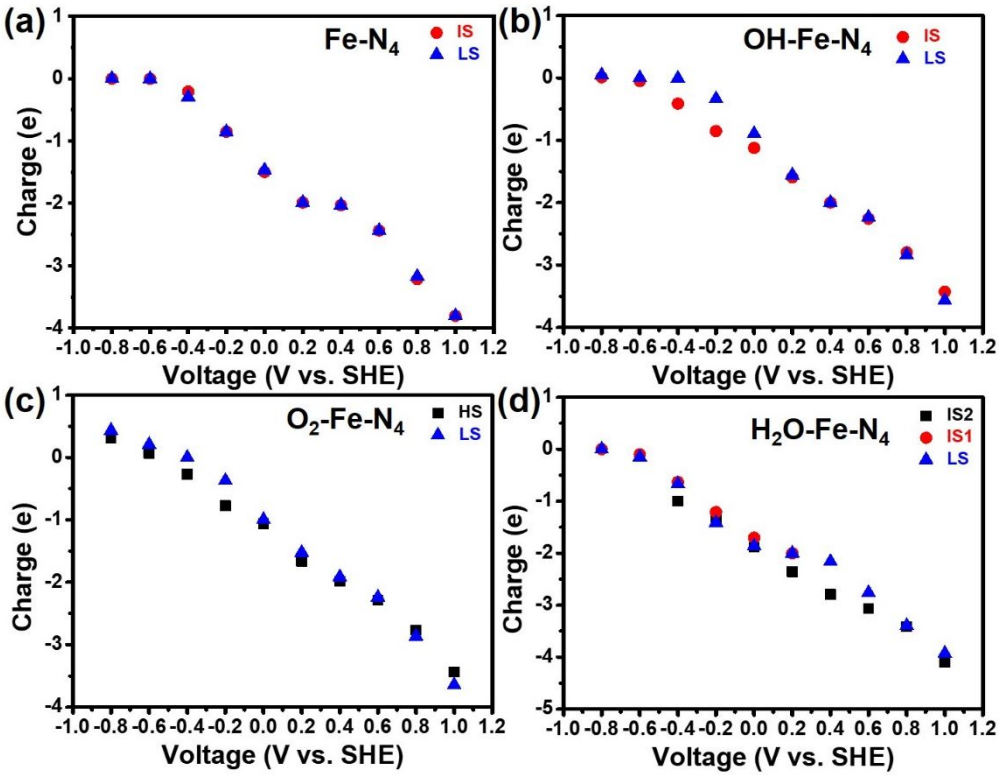

Figure S3. The surface charge for various spin states of Fe-N_4 (a), OH-Fe-N_4 (b), O_2-Fe-N_4 (c), and H_2O-Fe-N_4 (d) systems at different potentials.

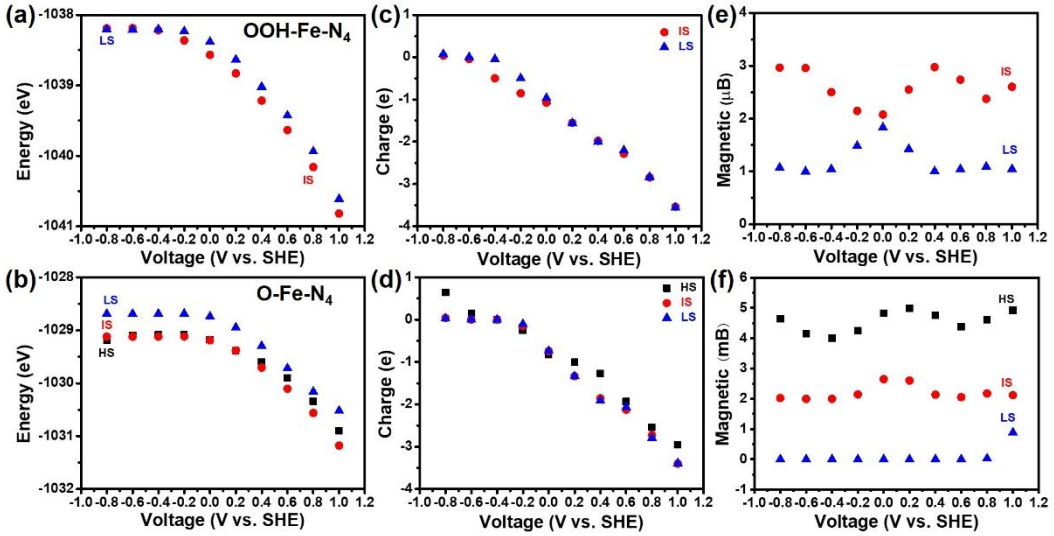

Figure S4. The energy (a), the surface charge (c), and the spin moment (e) for various spin states of the OOH-Fe-N_4 system at different potentials. The energy (b), the surface charge (d), and the spin moment (f) for various spin states of the O-Fe-N_4 system at different potentials.

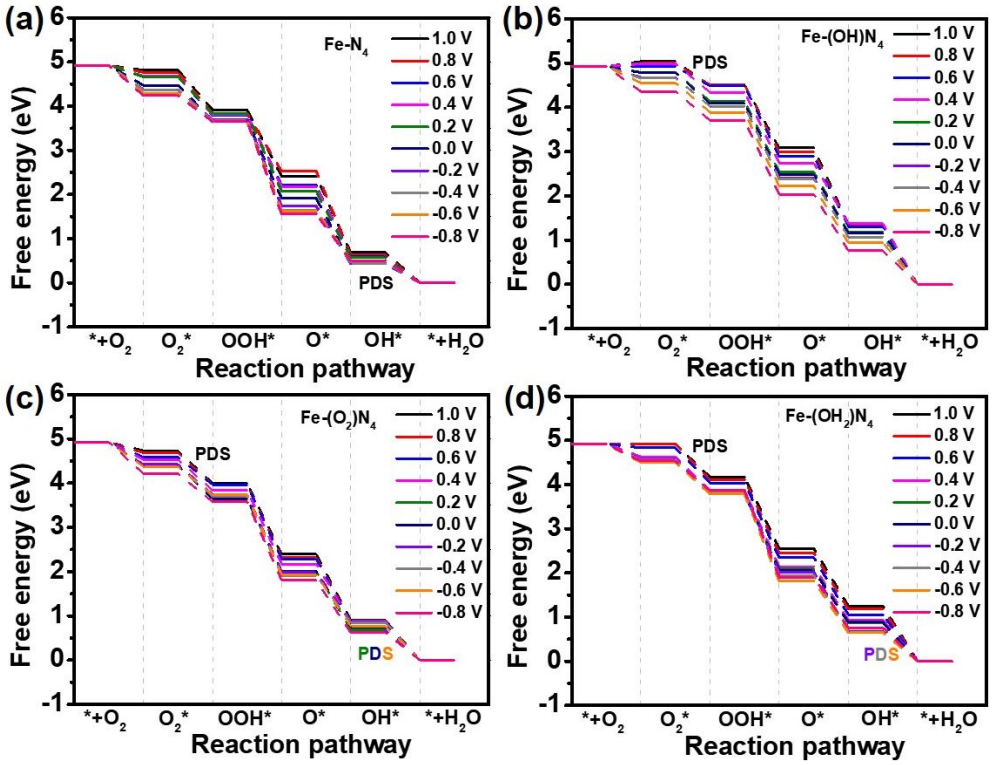

Figure S5. The potential-dependent ORR free energy diagram of the Fe-N_4 (a), Fe-$(O_2)N_4$ (b), Fe-$(O_2)N_4$ (c), and Fe-$(OH_2)N_4$ (d) active moieties.

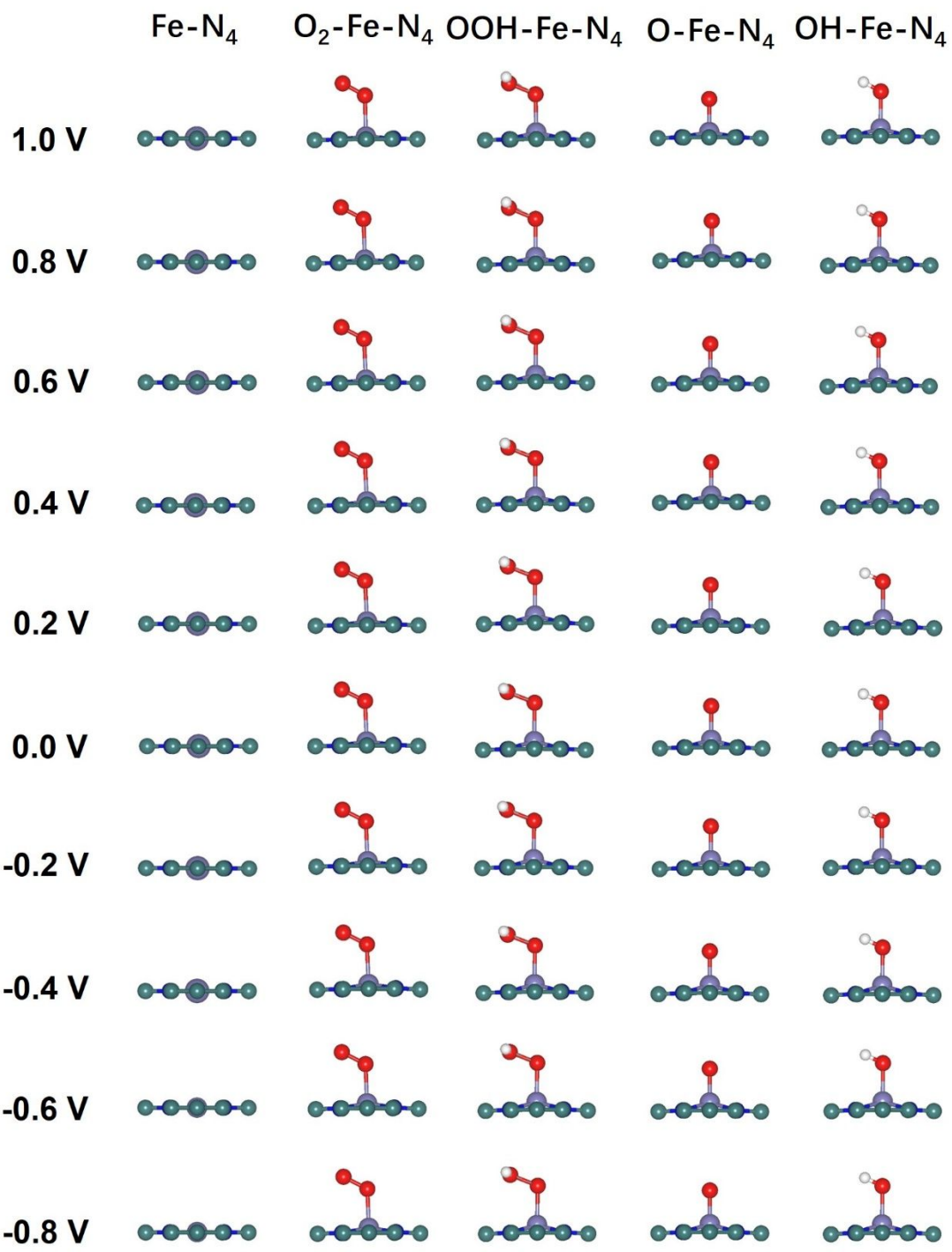

Figure S6. The ground state configurations of Fe-N_4, O_2-Fe-N_4, OOH-Fe-N_4, O-Fe-N_4, and OH-Fe-N_4 systems at different potentials.

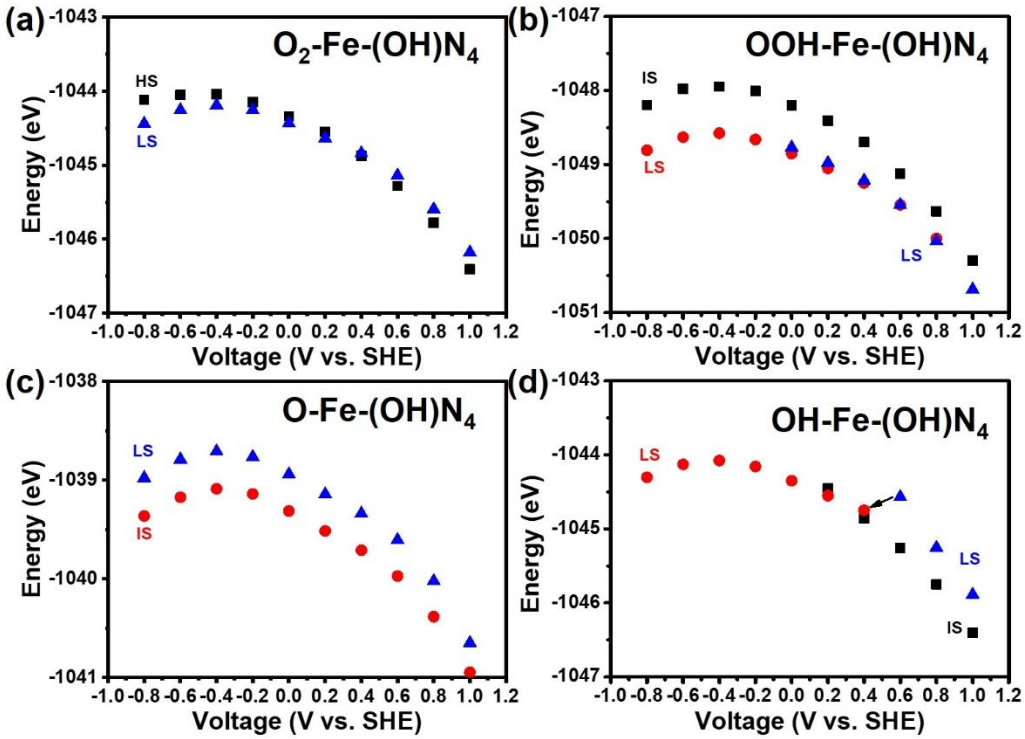

Figure S7. The potential-dependent energies of O_2-Fe-(OH)N_4 (a), OOH-Fe-(OH)N_4 (b), O-Fe-(OH)N_4 (c), and OH-Fe-(OH)N_4 (d) at different spin states.

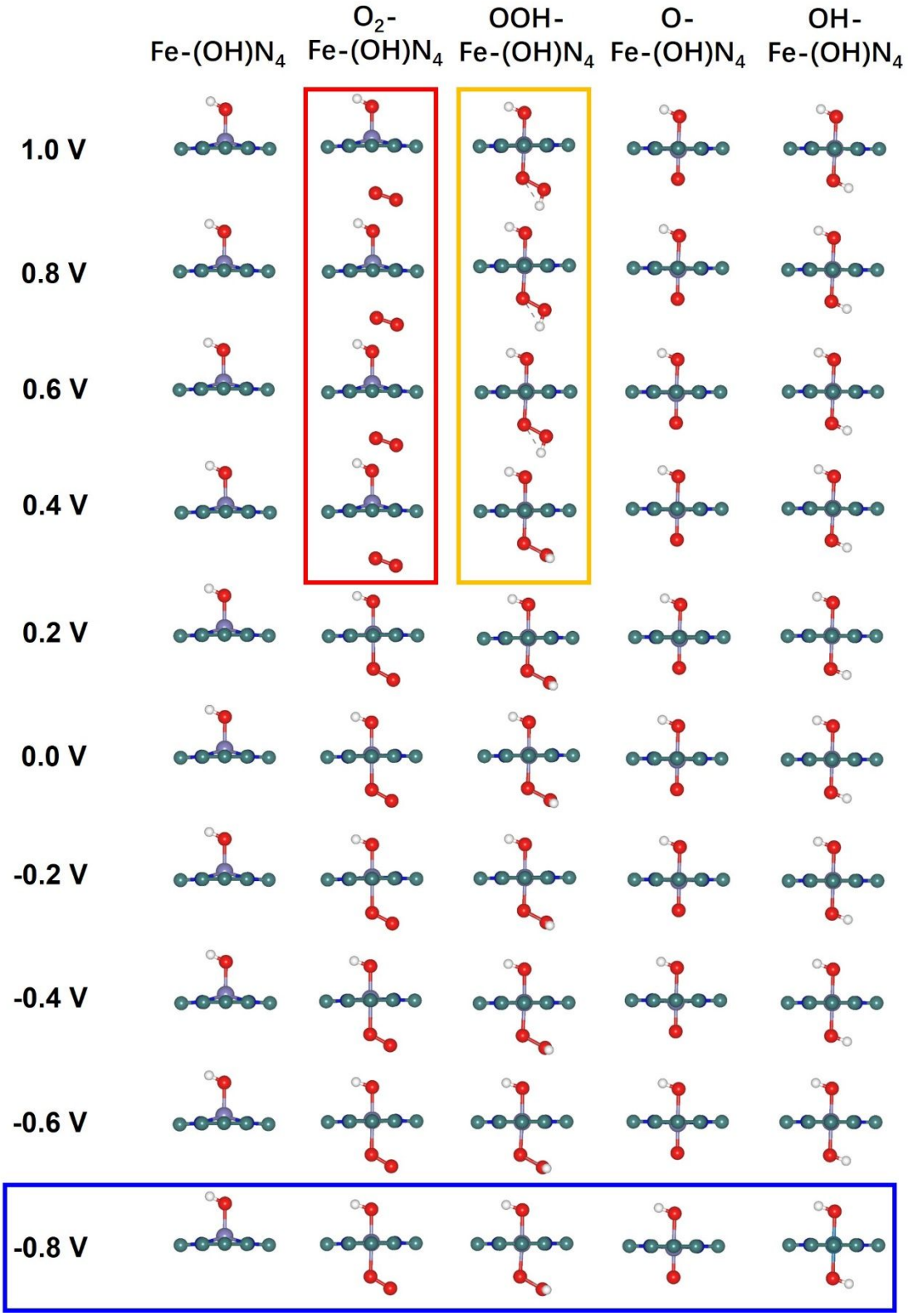

Figure S8. The ground state configurations of Fe-(OH)N_4, O_2-Fe-(OH)N_4, OOH-Fe-(OH)N_4, O-Fe-(OH)N_4, and OH-Fe-(OH)N_4 systems at different potentials.

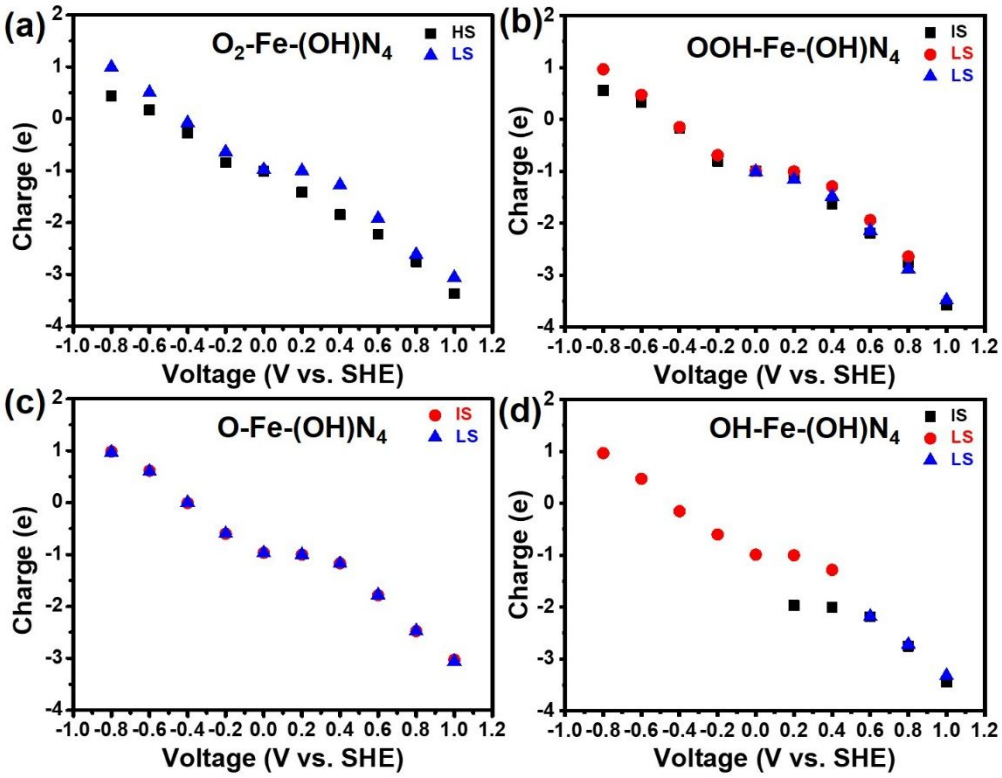

Figure S9. The surface charge for various spin states of O_2-Fe-$(OH)N_4$ (a), OOH-Fe-$(OH)N_4$ (b), O-Fe-$(OH)N_4$ (c), and OH-Fe-$(OH)N_4$ (d) systems at different potentials.

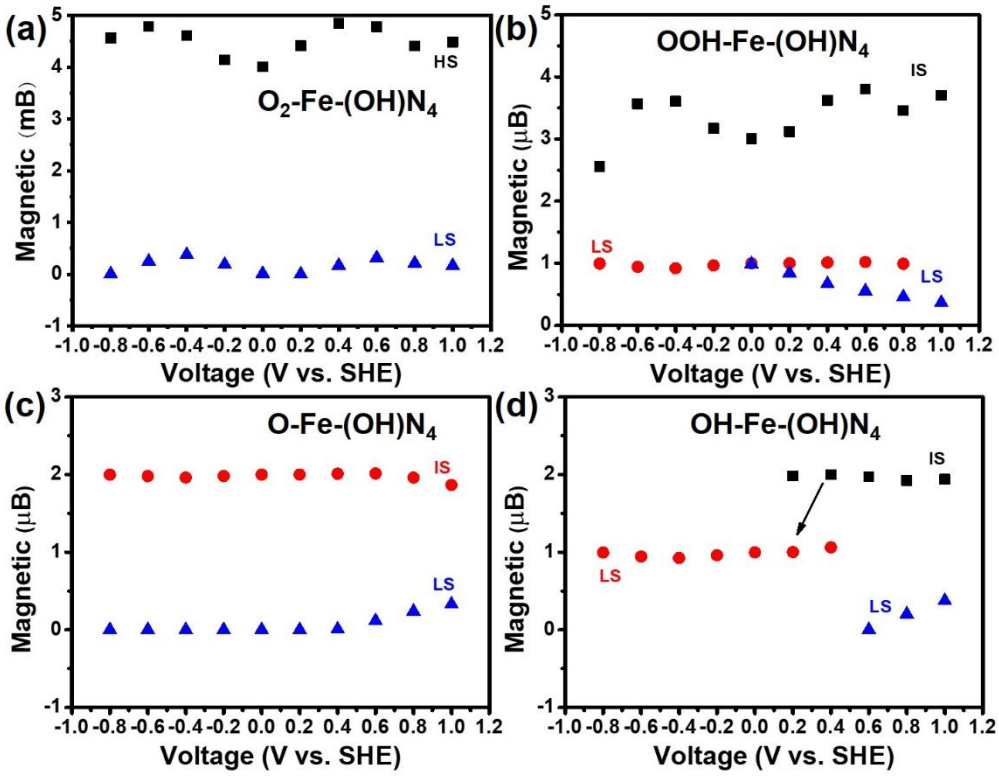

Figure S10. The spin moment for various spin states of O_2-Fe-(OH)N_4 (a), OOH-Fe-(OH)N_4 (b), O-Fe-(OH)N_4 (c), and OH-Fe-(OH)N_4 (d) systems at different potentials.

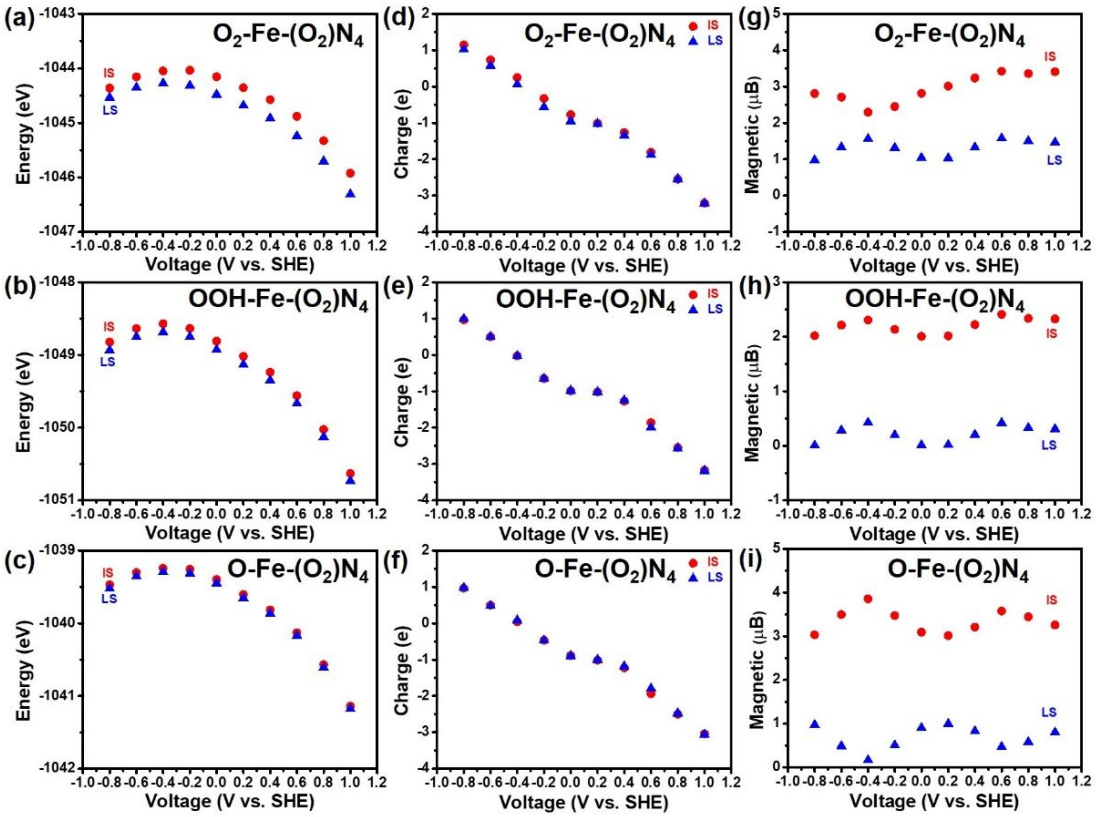

Figure S11. The energy for various spin states of O_2-Fe-(O_2)N_4 (a), OOH-Fe-(O_2)N_4 (b), and O-Fe-(O_2)N_4 (c) systems at different potentials. The surface charge for various spin states of O_2-Fe-(O_2)N_4 (d), OOH-Fe-(O_2)N_4 (e), and O-Fe-(O_2)N_4 (f) systems at different potentials. The spin moment for various spin states of O_2-Fe-(O_2)N_4 (g), OOH-Fe-(O_2)N_4 (h), and O-Fe-(O_2)N_4 (i) systems at different potentials.

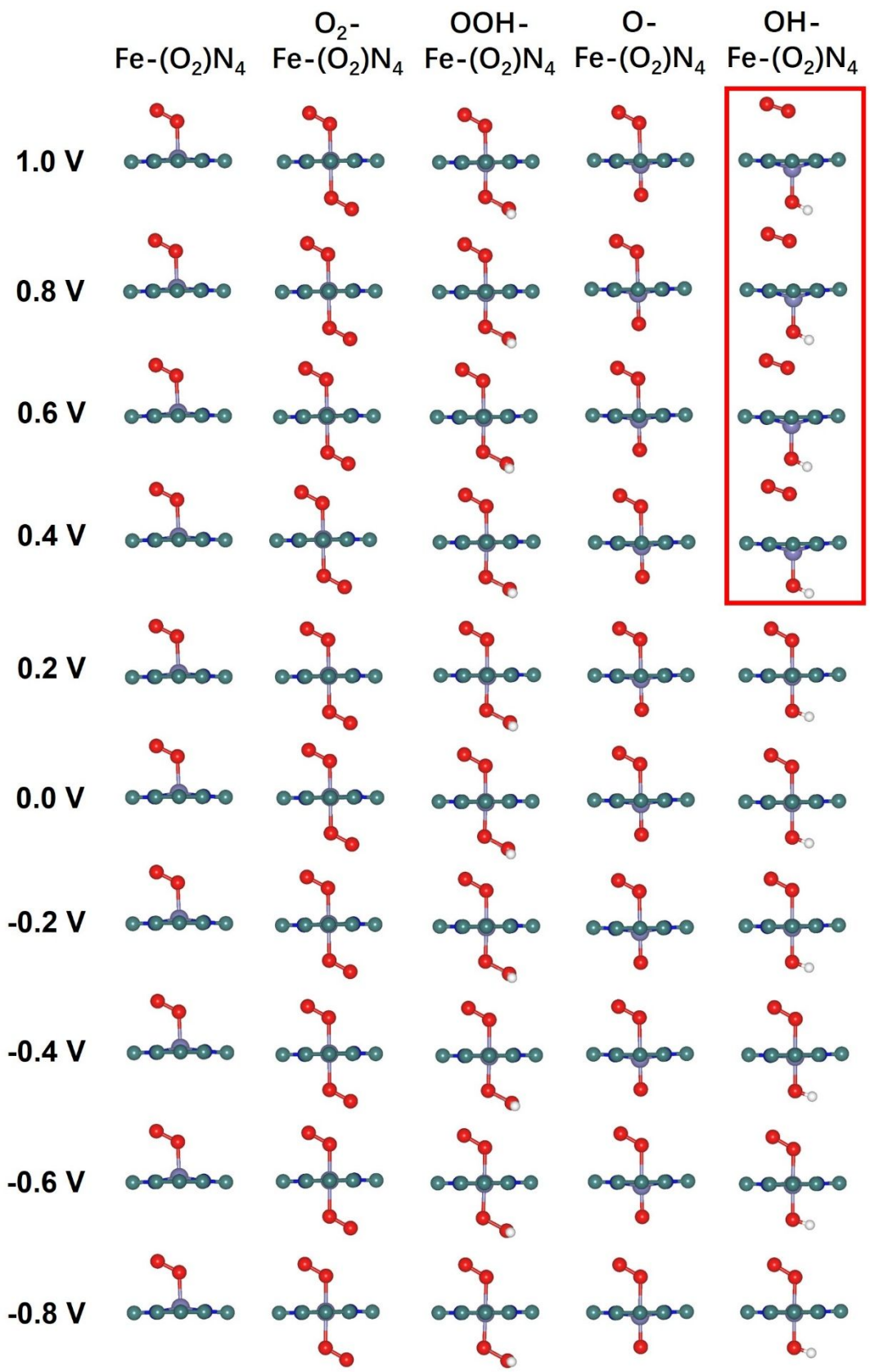

Figure S12. The ground state configurations of Fe-$(O_2)N_4$, O_2-Fe-$(O_2)N_4$, OOH-Fe-$(O_2)N_4$, O-Fe-$(O_2)N_4$, and OH-Fe-$(O_2)N_4$ systems at different potentials.

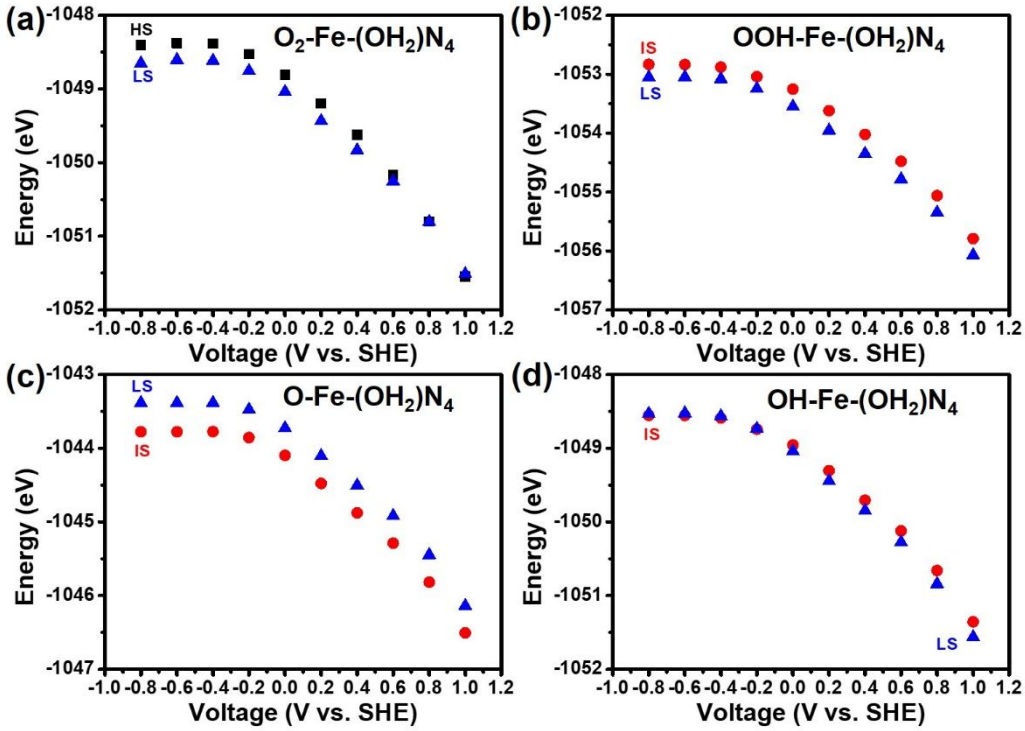

Figure S13. The energy for various spin states of O_2-Fe-$(OH_2)N_4$ (a), OOH-Fe-$(OH_2)N_4$ (b), O-Fe-$(OH_2)N_4$ (c), and OH-Fe-$(OH_2)N_4$ (d) systems at different potentials.

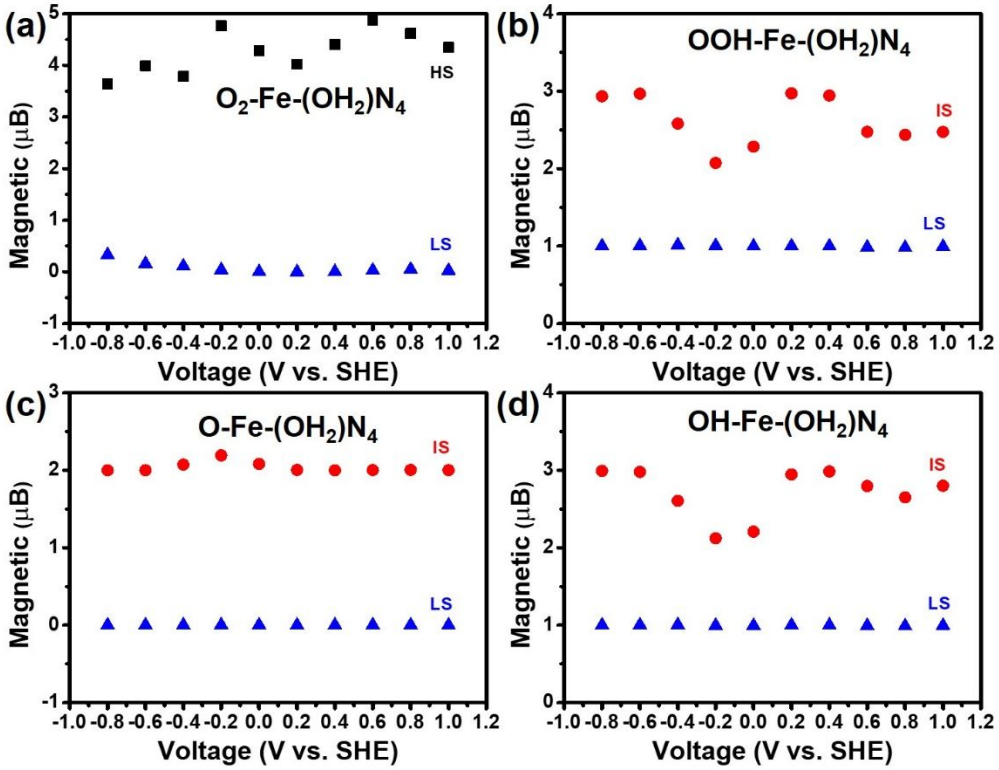

Figure S14. The spin moment for various spin states of O_2-Fe-$(OH_2)N_4$ (a), OOH-Fe-$(OH_2)N_4$ (b), O-Fe-$(OH_2)N_4$ (c), and OH-Fe-$(OH_2)N_4$ (d) systems at different potentials.

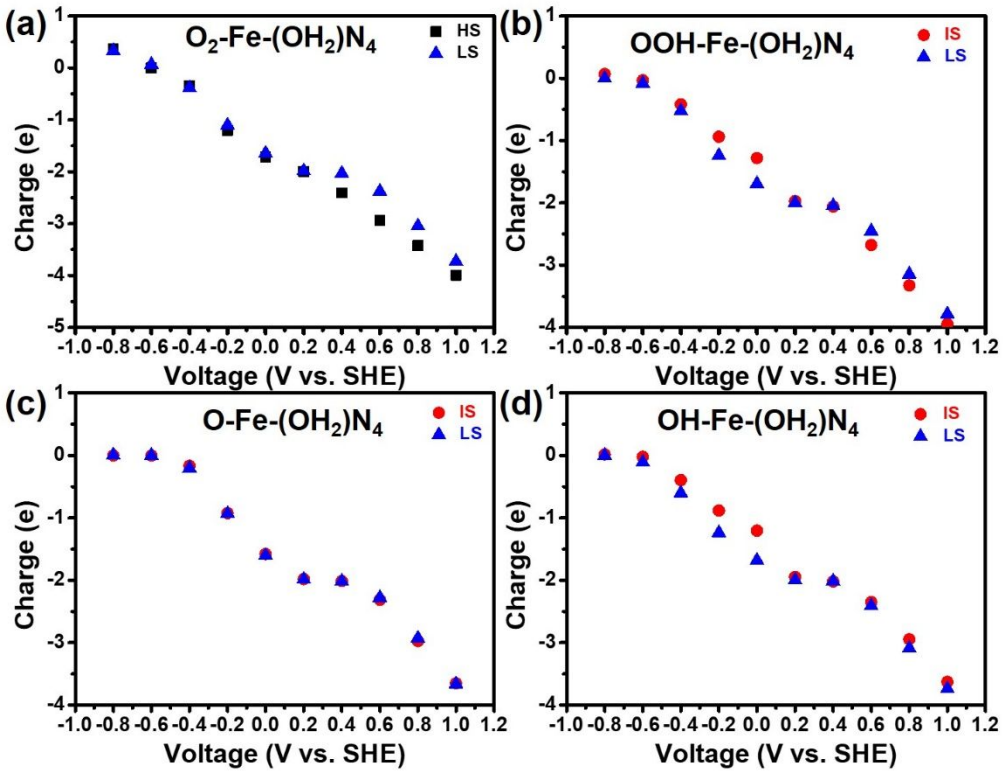

Figure S15. The surface charge for various spin states of O_2-Fe-$(OH_2)N_4$ (a), OOH-Fe-$(OH_2)N_4$ (b), O-Fe-$(OH_2)N_4$ (c), and OH-Fe-$(OH_2)N_4$ (d) systems at different potentials.

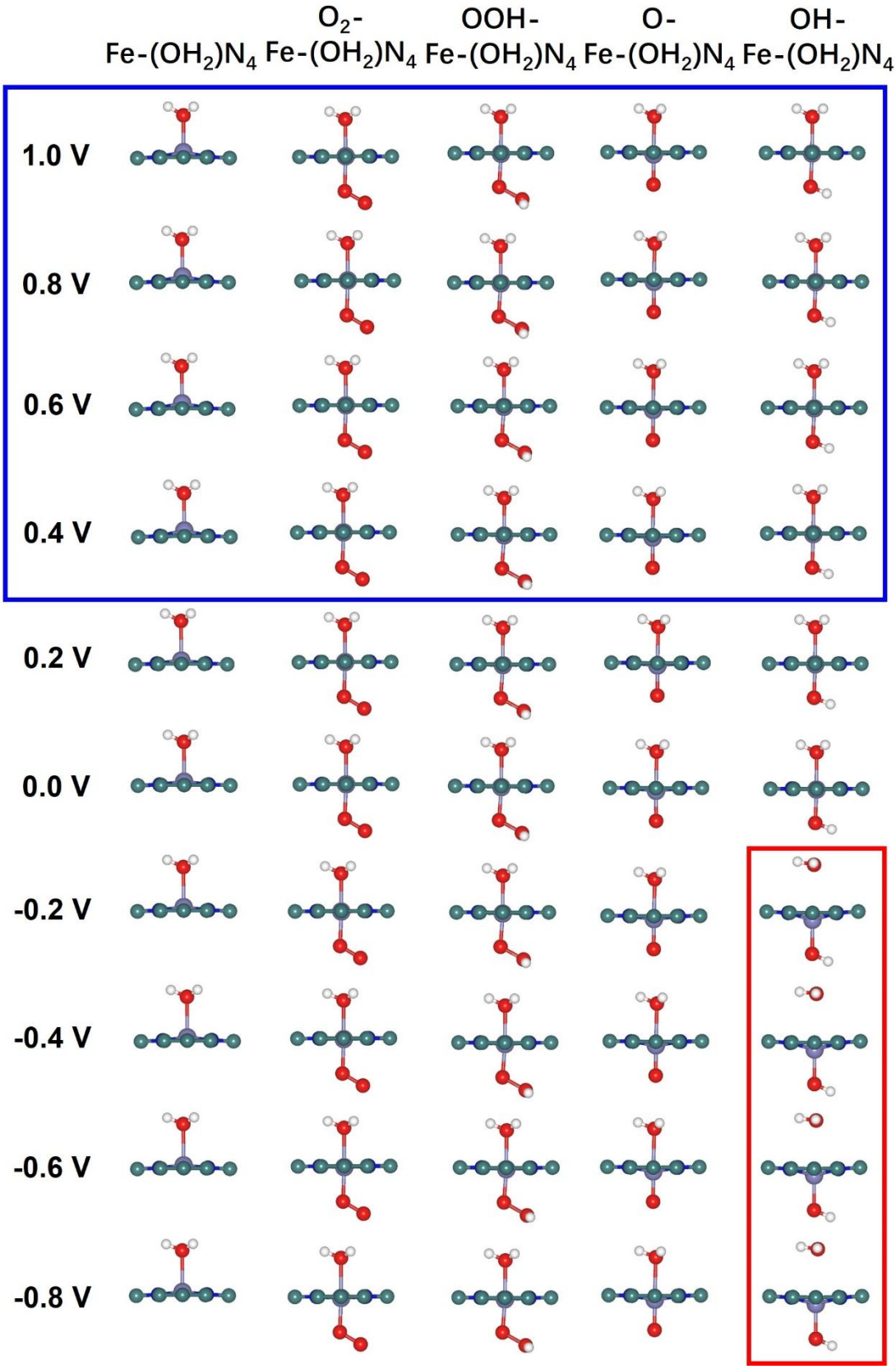

Figure S16. The ground state configurations of Fe-$(OH_2)N_4$, O_2-Fe-$(OH_2)N_4$, OOH-Fe-$(OH_2)N_4$, O-Fe-$(OH_2)N_4$, and OH-Fe-$(OH_2)N_4$ systems at different potentials.

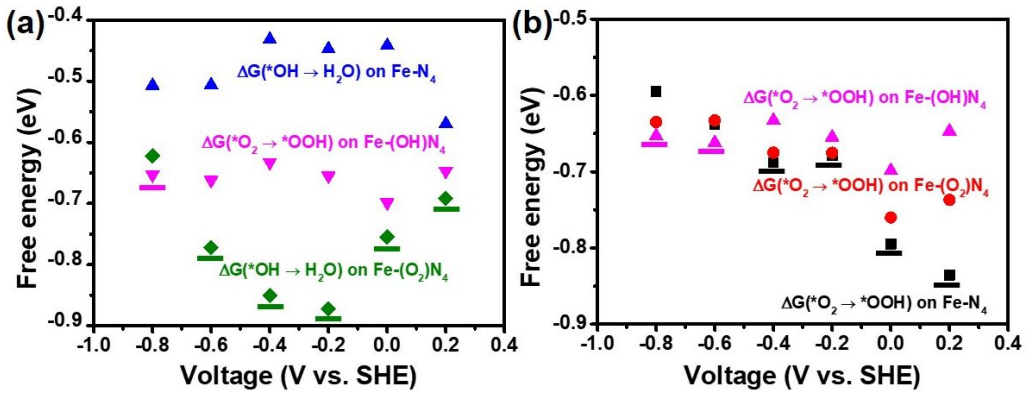

Figure S17. (a) Free energy changes (ΔG) of *OH and $*O_2$ competitive protonation in the OH-Fe-$(O_2)N_4$ system at different potentials. (b) Free energy changes of $*O_2$ protonation at the Fe-N_4, Fe-$(O_2)N_4$, and Fe-$(OH_2)N_4$ active moieties.

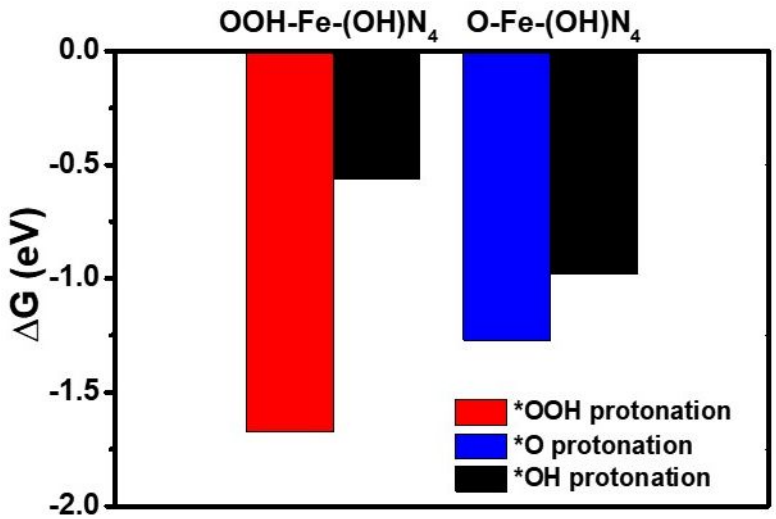

Figure S18. The competitive protonation of reaction intermediates (*OOH or *O) with *OH in the OOH-Fe-$(OH)N_4$ and O-Fe-$(OH)N_4$ systems.

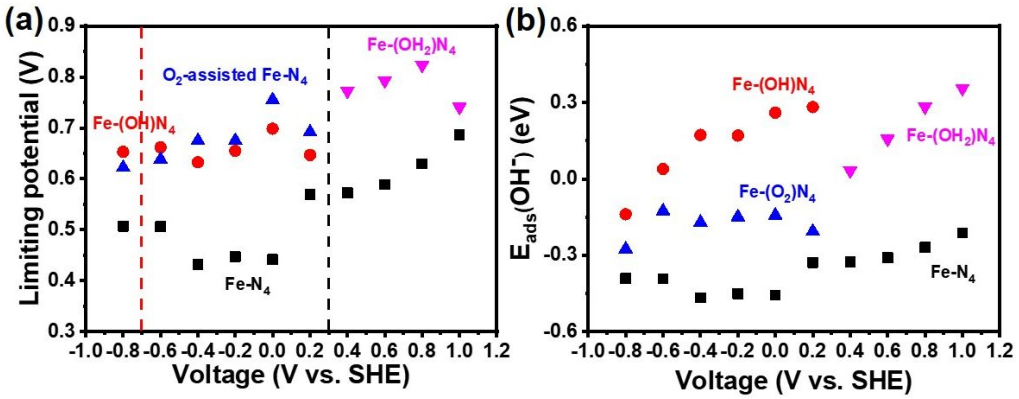

Figure S19. (a) The limiting potentials (U_L) of the ORR on the Fe-N_4, Fe-$(OH_2)N_4$, and Fe-$(OH)N_4$ active moieties at different potentials. (b) The adsorption energy of OH^- on the Fe-N_4, Fe-$(O_2)N_4$, Fe-$(OH)N_4$, and Fe-$(OH_2)N_4$ moieties.

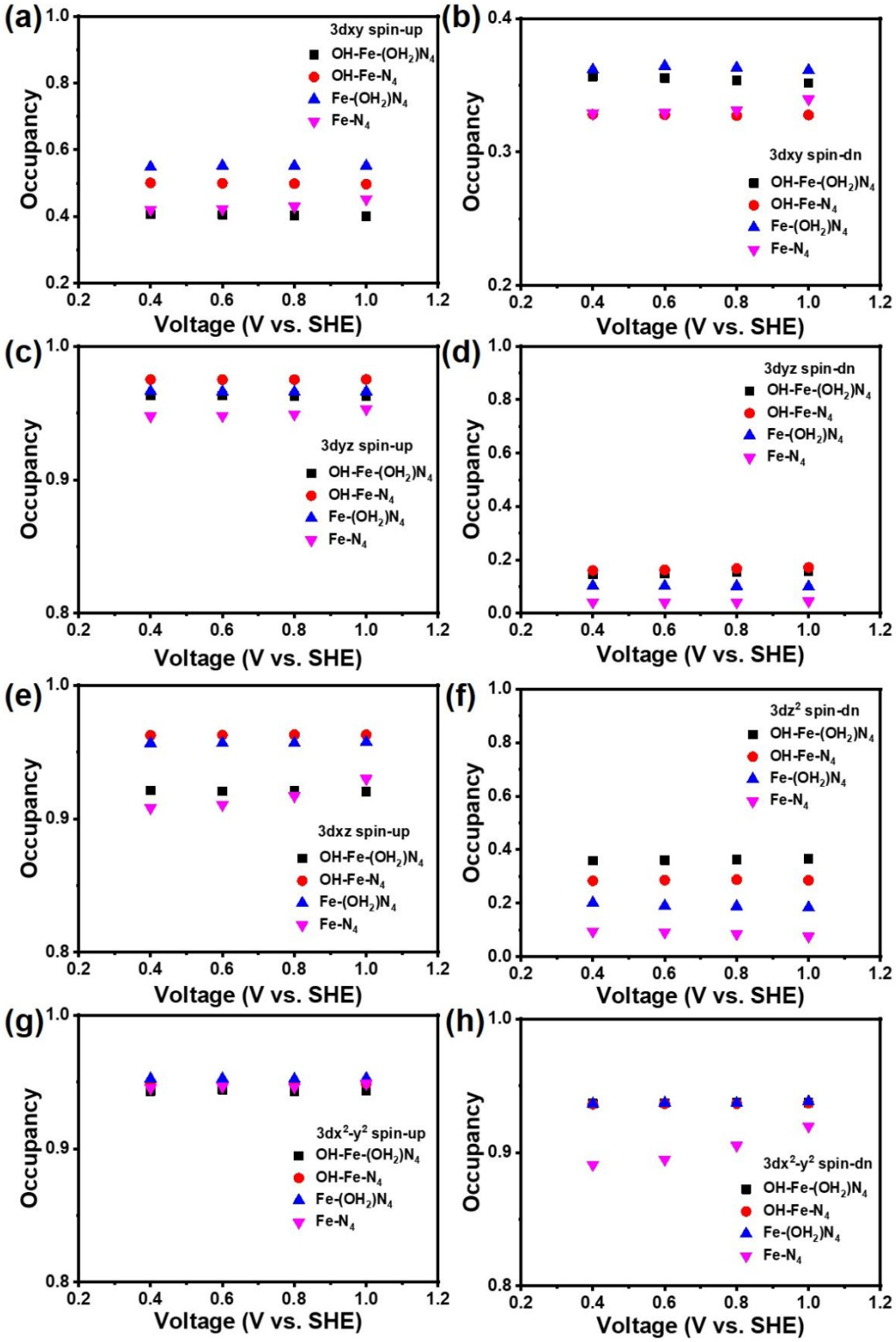

Figure S20. The electron occupancy of Fe 3dxy (spin-up) (a), Fe 3dxy (spin-dn) (b), Fe 3dyz (spin-up) (c), Fe 3dyz (spin-dn) (d), Fe 3dxz (spin-up) (e), Fe $3dz^2$ (spin-dn) (f), Fe $3dx^2$-y^2 (spin-up) (g), and Fe $3dx^2$-y^2 (spin-dn) (h) states in the Fe-N_4, Fe-$(OH_2)N_4$, OH-Fe-N_4, and OH-Fe-$(OH_2)N_4$ systems at the potential ≥0.4 V.

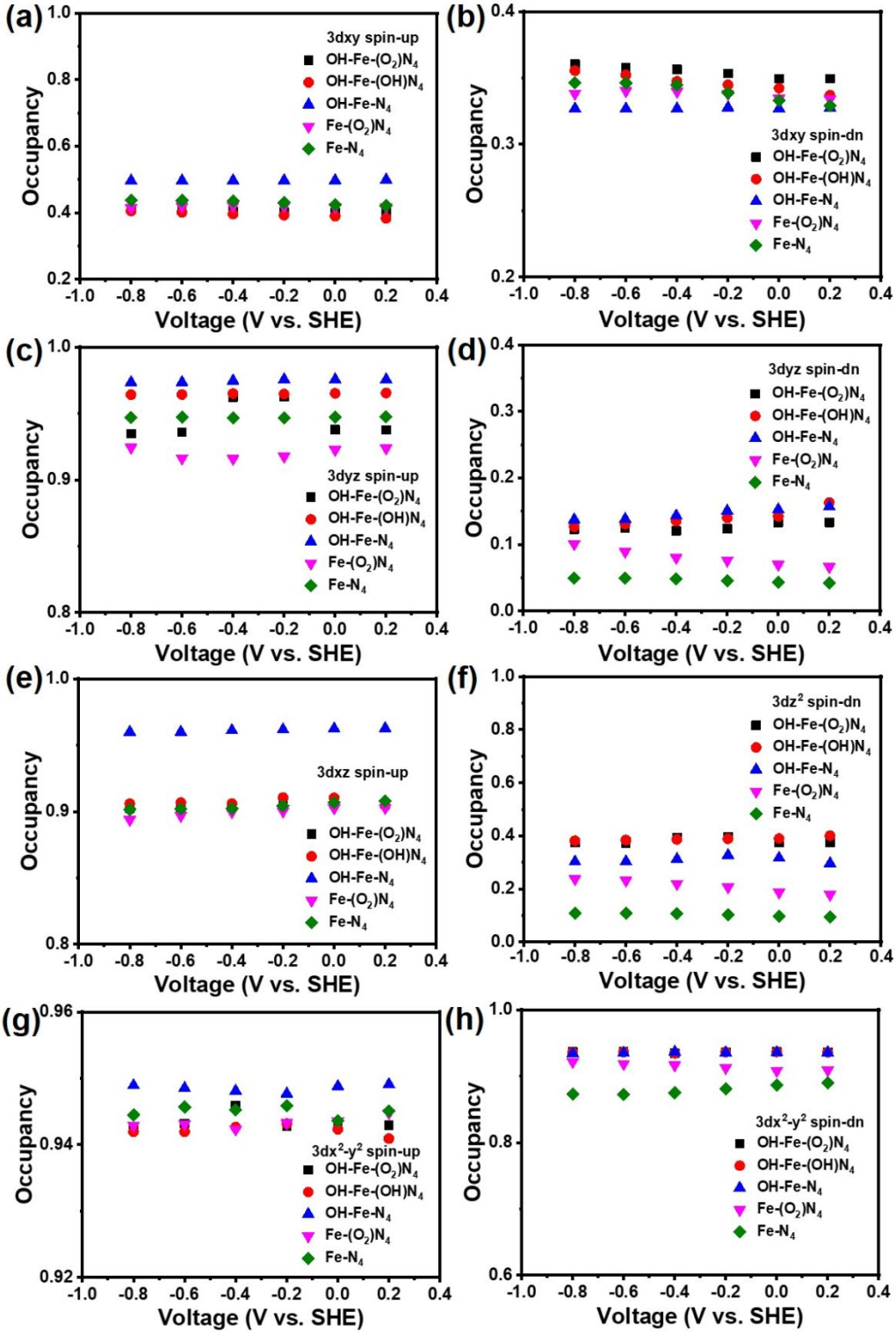

Figure S21. The electron occupancy of Fe 3dxy (spin-up) (a), Fe 3dxy (spin-dn) (b), Fe 3dyz (spin-up) (c), Fe 3dyz (spin-dn) (d), Fe 3dxz (spin-up) (e), Fe $3dz^2$ (spin-dn) (f), Fe $3dx^2$-y^2 (spin-up) (g), and Fe $3dx^2$-y^2 (spin-dn) (h) states in the Fe-N_4, Fe-$(O_2)N_4$, OH-Fe-N_4, OH-Fe-$(OH)N_4$, and OH-Fe-$(OH_2)N_4$ systems at the potential ≤0.2 V.

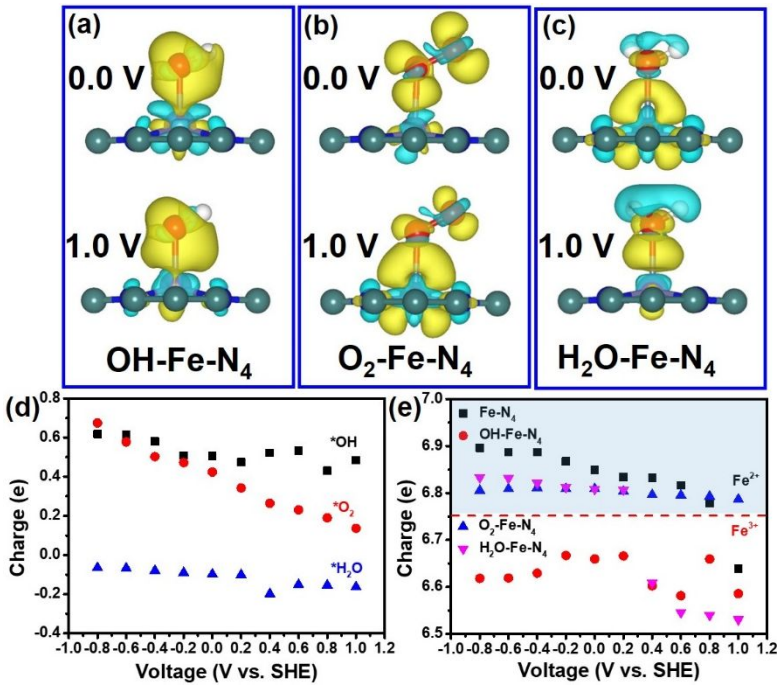

Figure S22. The charge density difference of OH-Fe-N_4 (a), O_2-Fe-N_4 (b), and H_2O-Fe-N_4 (c) systems. The Bader charge of *OH, *O_2, *H_2O (d), and Fe site (e) in Fe-N_4, OH-Fe-N_4, O_2-Fe-N_4, and H_2O-Fe-N_4 systems.

Note 1. The ground state of O_2-Fe-(OH)N_4, OOH-Fe-(OH)N_4, O-Fe-(OH)N_4, and OH-Fe-(OH)N_4 systems.

When the O_2 molecule adsorbed on the Fe-(OH)N_4 moiety, the potential-dependent energies of the HS and LS states are presented in Figure S7a. In the potential window from 0.4 to 1.0 V, the HS state becomes the ground state, and O_2 is not directly bound to Fe-(OH)N_4 moiety due to the weak interaction between O_2 and Fe-(OH)N_4 moiety (Figure S8). But the LS state with O_2 and Fe-(OH)N_4 moiety tight connection is more stable in the potential window from –0.8 to 0.2 V, due to the AFM exchange interaction between O_2 and Fe-(OH)N_4 moiety (Figure S8). The surface charge of the HS state is slightly less than the surface charge of the LS state at the O_2-Fe-(OH)N_4 system (Figure S9a and S10a). For the OOH-Fe-(OH)N_4 system, the energy of the LS state is lower than that of the IS state with no significant fluctuations in the surface charge between the LS and the IS states (Figure S7b and S9). When the potential is ≥0.4 V, the spin moment of the LS state gradually decays from 1.00 to 0.37 μB with the deflexion of *OOH intermediate configuration (Figure S8 and S10b). For the O-Fe-(OH)N_4 system, the energy of the IS state is lower than that of the LS state (Figures S7c and S10c), and the surface charges of the IS and LS states are essentially the same (Figure S9). For the OH-Fe-(OH)N_4 system, the spin crossover effect is located at the potential of 0.4 V (Figure S7d and S10d). From the potential-dependent energies of the LS and IS states, the IS state of the OH-Fe-(OH)N_4 system is more stable than the LS state at the potential ≥0.4 V. When the potential is ≤0.2 V, the energy of the LS state is lower than that of the IS state in the OH-Fe-(OH)N_4 system. These results are used to assess the ORR activity and reaction mechanism at the Fe-(OH)N_4 moiety.

Note 2. The ground state of O_2-Fe-$(O_2)N_4$, OOH-Fe-$(O_2)N_4$, and O-Fe-$(O_2)N_4$ systems.

When the oxygenated species (*O_2, *OOH, and *O) are adsorbed on the Fe-$(O_2)N_4$ moiety, the potential-dependent energies of O_2-Fe-$(O_2)N_4$, OOH-Fe-$(O_2)N_4$, and O-Fe-$(O_2)N_4$ systems show that the LS state is more stable than the IS state at all potentials (Figure S11a-c). The difference in surface charge between the IS state and the LS state is not significant (Figure S11d-f). The spin moment for various spin states of O_2-Fe-$(O_2)N_4$, OOH-Fe-$(O_2)N_4$, and O-Fe-$(O_2)N_4$ systems at different potentials are shown in Figure S11g-i. The ground state configurations of Fe-$(O_2)N_4$, O_2-Fe-$(O_2)N_4$, OOH-Fe-$(O_2)N_4$, O-Fe-$(O_2)N_4$, and OH-Fe-$(O_2)N_4$ systems at different potentials are shown in Figure S12. These results are used to assess the ORR activity and reaction mechanism at the Fe-$(O_2)N_4$ moiety.

Note 3. The ground state of O_2-Fe-$(OH_2)N_4$, OOH-Fe-$(OH_2)N_4$, O-Fe-$(OH_2)N_4$, and OH-Fe-$(OH_2)N_4$ systems.

For the Fe-$(OH_2)N_4$ moiety, the O_2 molecule can adsorb directly on the single-atom Fe site to form the O_2-Fe-$(OH_2)N_4$ system. The energy of the LS state is lower than that of the IS state at the potential ≤0.8 V (Figure S13a). The HS state becomes the ground state at 1.0 V by a small energy drop (Figure S13a and S14a). From the potential-dependent energies of the OOH-Fe-$(OH_2)N_4$ system, the LS state is also more stable than the IS state at all potentials (Figure S13b and S14b). When the OOH-Fe-$(OH_2)N_4$ is converted to O-Fe-$(OH_2)N_4$ system, the IS state exhibits an energetically favorable state than the LS state at all potentials (Figure S13c and S14c). For the OH-Fe-$(OH_2)N_4$ system, the potential-dependent energies of the IS and the LS state cross at the potential –0.2 V, implying that the LS state is the ground state at the potential ≥ 0.0 V, while the IS state transitions to the ground state at the potential ≤ –0.2 V (Figure S13d and S14d). For the O_2-Fe-$(OH_2)N_4$, OOH-Fe-$(OH_2)N_4$, O-Fe-$(OH_2)N_4$, and OH-Fe-$(OH_2)N_4$ systems, the surface charges in the different spin states do not differ significantly, despite the large differences in spin moments among the different spin states (Figure S15). We found that the geometric configuration of the OH-Fe-$(OH_2)N_4$ system changes significantly at the potential ≤–0.2 V (Figure S16). The axially ligated H_2O is desorbed from the single-atom Fe site, indicating that the structure of the Fe-$(OH_2)N_4$ moiety may be destroyed during the ORR at the potential ≤–0.2 V. These results are used to assess the ORR activity and reaction mechanism at the Fe-$(OH_2)N_4$ moiety.

Table S1. The free energy data of the ORR on the Fe-N_4 moiety at the potential (U) window from –0.8 to 1.0 V (*vs.* SHE).

U (V)	O_2 (eV)	*O_2	*OOH	O*	*OH	H_2O	U_L
1.0	4.92	4.81	3.92	2.41	**0.69**	**0**	0.69
0.8	4.92	4.78	3.84	2.52	**0.63**	**0**	0.63
0.6	4.92	4.67	3.80	2.21	**0.59**	**0**	0.59
0.4	4.92	4.68	3.80	2.18	**0.57**	**0**	0.57
0.2	4.92	4.67	3.83	2.07	**0.57**	**0**	0.57
0.0	4.92	4.47	3.68	1.91	**0.44**	**0**	0.44
–0.2	4.92	4.38	3.70	1.74	**0.45**	**0**	0.45
–0.4	4.92	4.36	3.68	1.64	**0.43**	**0**	0.43
–0.6	4.92	4.28	3.65	1.63	**0.51**	**0**	0.51
–0.8	4.92	4.24	3.65	1.56	**0.51**	**0**	0.51

Notes: The bold data are associated with the value of the potential-determining step (PDS). The red data is the limiting potential (U_L) of ORR.

Table S2. The free energy data of the ORR on the Fe-(OH)N_4 moiety at the potential (U) window from –0.8 to 1.0 V (*vs.* SHE).

U (V)	O_2 (eV)	*O_2	*OOH	O*	*OH	H_2O	U_L (V)
1.0	4.92	**5.04**	**4.50**	3.08	1.35	0	0.54
0.8	4.92	**4.99**	**4.51**	2.99	1.32	0	0.48
0.6	4.92	**4.92**	**4.48**	2.89	1.31	0	0.44
0.4	4.92	**4.99**	**4.34**	2.74	1.37	0	0.65
0.2	4.92	**4.79**	**4.14**	2.54	1.18	0	0.65
0.0	4.92	**4.79**	**4.09**	2.49	1.16	0	0.70
–0.2	4.92	**4.67**	**4.02**	2.41	1.07	0	0.65
–0.4	4.92	**4.66**	**4.03**	2.38	1.07	0	0.63
–0.6	4.92	**4.55**	**3.89**	2.22	0.94	0	0.66
–0.8	4.92	**4.35**	**3.70**	2.03	0.76	0	0.65

Notes: The bold data are associated with the value of the potential-determining step (PDS). The red data is the limiting potential (U_L) of ORR.

Table S3. The free energy data of the ORR on the Fe-(O_2)N_4 moiety at the potential (U) window from –0.8 to 1.0 V (*vs.* SHE).

U (V)	O_2 (eV)	*O_2	*OOH	O*	*OH	H_2O	U_L (V)
1.0	4.92	**4.73**	**4.00**	2.40	0.91	0	0.73
0.8	4.92	**4.69**	**3.97**	2.33	0.86	0	0.72
0.6	4.92	**4.59**	**3.96**	2.28	0.84	0	0.63
0.4	4.92	**4.53**	**3.84**	2.17	0.88	0	0.69
0.2	4.92	4.39	3.65	2.00	**0.69**	**0**	0.69
0.0	4.92	4.40	3.64	2.0	**0.75**	**0**	0.75
–0.2	4.92	**4.42**	**3.75**	1.99	0.87	0	0.67
–0.4	4.92	**4.37**	**3.70**	1.91	0.85	0	0.67
–0.6	4.92	**4.37**	**3.74**	1.93	0.77	0	0.63
–0.8	4.92	4.21	3.58	1.80	**0.62**	**0**	0.62

Notes: The bold data are associated with the value of the potential-determining step (PDS). The red data is the limiting potential (U_L) of ORR.

Table S4. The free energy data of the ORR on the Fe-$(OH_2)N_4$ moiety at the potential (U) window from –0.8 to 1.0 V (*vs.* SHE).

U (V)	O_2 (eV)	$*O_2$	*OOH	O*	*OH	H_2O	U_L (V)
1.0	4.92	**4.91**	**4.17**	2.56	1.25	0	0.74
0.8	4.92	**4.93**	**4.11**	2.45	1.18	0	0.82
0.6	4.92	**4.83**	**4.04**	2.35	1.05	0	0.79
0.4	4.92	**4.63**	**3.86**	2.14	0.93	0	0.77
0.2	4.92	**4.57**	**3.80**	2.09	0.87	0	0.77
0.0	4.92	**4.57**	**3.80**	2.07	0.88	0	0.77
–0.2	4.92	4.58	3.81	2.02	**0.68**	**0**	0.68
–0.4	4.92	4.56	3.81	1.94	**0.65**	**0**	0.65
–0.6	4.92	4.51	3.78	1.82	**0.65**	**0**	0.65
–0.8	4.92	**4.53**	**3.86**	1.90	0.76	0	0.67

Notes: The bold data are associated with the value of the potential-determining step (PDS). The red data is the limiting potential (U_L) of ORR.

REFERENCES

(1) G. Kresse; Furthmu¨ller, J. Efficiency of ab-initio Total Energy Calculations for Metals and Semiconductors Using a Plane-Wave Basis Set. *Comp. Mater, Sci.* **1996,** *6*, 15-50.

(2) G. Kresse; Furthmu¨ller, J. Efficient Iterative Schemes for ab initio Total-Energy Calculations Using a Plane-Wave Basis Set. *Phys. Rev. B* **1996,** *54*, 11169-11186.

(3) Blochl, P. E. Projector Augmented-Wave Method. *Phys. Rev. B* **1994,** *50*, 17953-17979.

(4) Perdew, J. P.; Burke, K.; Ernzerhof, M. Generalized Gradient Approximation Made Simple. *Phys. Rev. Lett.* **1996,** *77*, 3865-3868.

(5) Perdew, J. P.; Chevary, J. A.; Vosko, S. H.; Jackson, K. A.; Pederson, M. R.; Singh, D. J.; Fiolhais, C. Atoms, Molecules, Solids, and Surfaces: Applications of the Generalized Gradient Approximation for Exchange and Correlation. *Phys. Rev. B* **1992,** *46*, 6671-6687.

(6) Zhou, J.; Sun, Q. Magnetism of Phthalocyanine-Based Organometallic Single Porous Sheet. *J. Am. Chem. Soc.* **2011,** *133*, 15113-15119.

(7) Hutchison, P.; Rice, P. S.; Warburton, R. E.; Raugei, S.; Hammes-Schiffer, S. Multilevel Computational Studies Reveal the Importance of Axial Ligand for Oxygen Reduction Reaction on Fe-N-C Materials. *J. Am. Chem. Soc.* **2022,** *144*, 16524-16534.

(8) Liu, K.; Fu, J.; Lin, Y.; Luo, T.; Ni, G.; Li, H.; Lin, Z.; Liu, M. Insights into the Activity of Single-Atom Fe-N-C Catalysts for Oxygen Reduction Reaction. *Nat. Commun.* **2022,** *13*, 2075.

(9) Grimme, S. Semiempirical GGA-type Density Functional Constructed with a Long-Range Dispersion Correction. *J. Comput. Chem.* **2006,** *27*, 1787-1799.

(10) Mathew, K.; Kolluru, V. S. C.; Mula, S.; Steinmann, S. N.; Hennig, R. G. Implicit Self-Consistent Electrolyte Model in Plane-Wave Density-Functional Theory. *J. Chem. Phys.* **2019,** *151*, 234101.

(11) Mathew, K.; Sundararaman, R.; Letchworth-Weaver, K.; Arias, T. A.; Hennig, R. G. Implicit Solvation Model for Density-Functional Study of Nanocrystal Surfaces and Reaction Pathways. *J. Chem. Phys.* **2014,** *140*, 084106.

(12) Allen, J. P.; Watson, G. W. Occupation Matrix Control of d- and f-Electron Localisations Using DFT + U. *Phys. Chem. Chem. Phys.* **2014,** *16*, 21016-21031.

(13) Duan, Z.; Xiao, P. Simulation of Potential-Dependent Activation Energies in Electrocatalysis: Mechanism of O–O Bond Formation on RuO_2. *J. Phys. Chem. C* **2021,** *125*, 15243-15250.

(14) Nørskov, J. K.; Bligaard, T.; Logadottir, A.; Kitchin, J. R.; Chen, J. G.; Pandelov, S.; Stimming, U. Trends in the Exchange Current for Hydrogen Evolution. *J. Electrochem. Soc.* **2005,** *152*, J23-J26.

(15) Nørskov, J. K.; J. Rossmeisl; A. Logadottir; L. Lindqvist; J. R. Kitchin; T. Bligaard; Jo´nsson, H. Origin of the Overpotential for Oxygen Reduction at a Fuel-Cell Cathode. *J. Phys. Chem. B* **2004,** *108*, 17886-17892.

(16) Peterson, A. A.; Abild-Pedersen, F.; Studt, F.; Rossmeisl, J.; Nørskov, J. K. How Copper Catalyzes the Electroreduction of Carbon Dioxide into Hydrocarbon. *Energy Environ. Sci.* **2010,** *3*, 1311–1315.